Matter

CellPress

Article

X-ray-to-NIR multi-wavelength imaging through stochastic photoluminescence and compressed encoding

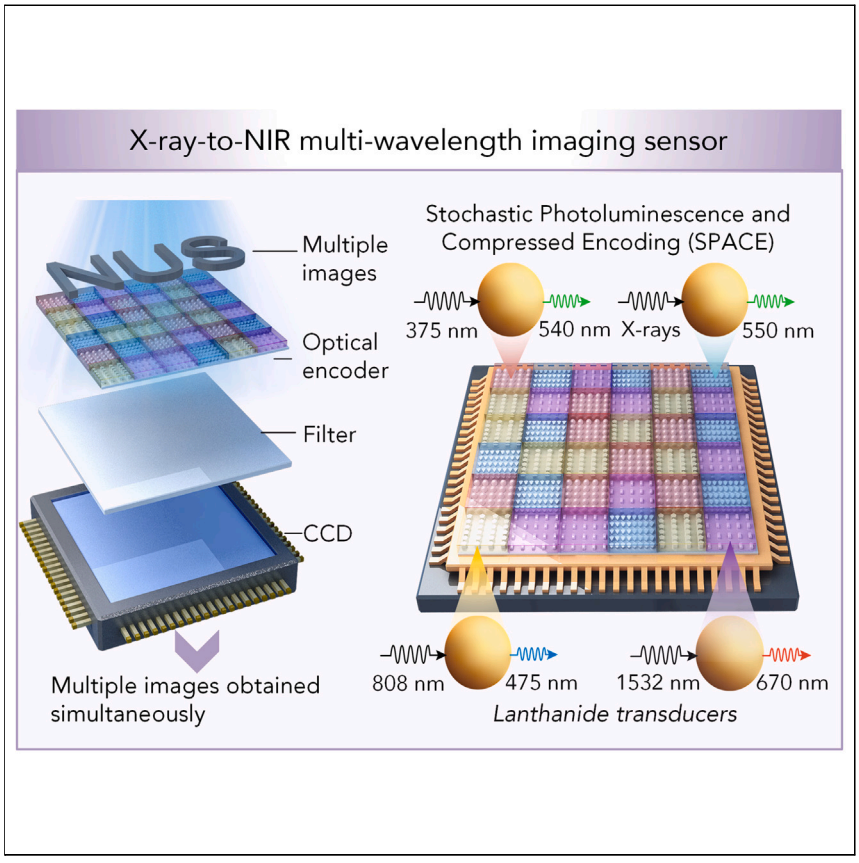

We report a new method for multi-wavelength imaging called stochastic photoluminescence and compressed encoding (SPACE), which employs multiple lanthanide transducers. This system enables the simultaneous capture of four distinct images, each tagged with different wavelengths: X-rays, UV, NIR I, and NIR II. Optical encoders then process these images in different sampling patterns, subsequently transmitting luminescence-based images to the CCD for detection. Ultimately, four complete images corresponding to each wavelength can be reconstructed from the encoded data captured by the CCD.

Luying Yi, Hong Qi Tan, Bo Hou, Xiaogang Liu

chmlx@nus.edu.sg

Highlights

"SPACE" with multiple lanthanide transducers enables multi-wavelength imager

Diverse scenes are encoded into a single image, reconstructed using algorithms

Channel expansion methods include number and thickness control of material layer

Multi-depth visualization and multi-spectrum X-ray imaging are obtained

6 **Development**
Practical, real world, technological considerations and constraints

Yi et al., Matter 7, 1–17
July 3, 2024
https://doi.org/10.1016/j.matt.2024.02.014

Please cite this article in press as: Yi et al., X-ray-to-NIR multi-wavelength imaging through stochastic photoluminescence and compressed encoding, Matter (2024), https://doi.org/10.1016/j.matt.2024.02.014

Matter

CellPress

Article

X-ray-to-NIR multi-wavelength imaging through stochastic photoluminescence and compressed encoding

Luying Yi,[1] Hong Qi Tan,[2] Bo Hou,[1] and Xiaogang Liu[1,3,4,*]

SUMMARY

Multi-wavelength imaging is crucial for gaining detailed insights into the multi-depth or multi-wavelength information present in the scenes. However, conventional methods often have limitations, like costly and bulky components restricted to specific wavelength ranges. Here, we introduce an imaging technique named "stochastic photoluminescence and compressed encoding," or SPACE. SPACE leverages randomly arrayed lanthanide transducers as photonic encoders to capture various excitation wavelengths in a single image, recorded by a charge-coupled device. This approach enables the reconstruction of multiple scenes from this encoded image across four wavelength channels: X-rays (0.089 nm), ultraviolet (375 nm), and two near-infrared bands (808 and 1,532 nm), with the ability to expand to more channels through multi-layer encoders. SPACE enables multi-channel imaging for depth visualization and multi-spectral X-ray analysis, offering broad multi-spectral sensitivity and on-chip compatibility. This makes it a versatile tool for applications in materials characterization, bioimaging, remote sensing, and astronomy.

INTRODUCTION

Multi-wavelength, multi-channel, and multi-depth imaging technologies have revolutionized scientific research and industrial applications, enabling precise three-dimensional reconstruction and comprehensive information representation of target objects.[1–5] These technologies capture unique characteristics of target objects across various wavelength bands, encompassing ultraviolet (UV), visible light, and infrared (IR) ranges. By employing diverse wavelengths of light to illuminate different sample sections, simultaneous multi-wavelength excitation permits the acquisition of multiple depth images. However, challenges arise from the sequential switching of excitation wavelengths and filters, leading to issues in terms of image acquisition speed and the inability to simultaneously observe synergistic and multi-depth information. Proposed solutions, involving complex beam splitting via multiple optical components, diffractive optical elements, metasurfaces, or multi-spectral filters, tend to escalate system dimensions, complexity, and costs.[6–9] Therefore, despite rapid advances in optical imaging and dispersive systems, their direct combination results in a cumbersome setup that hinders the practical implementation of multi-wavelength and multi-channel imaging. Moreover, most existing methods are limited to the visible band, and the realization of a multi-wavelength imaging system spanning near-IR (NIR; I and II), visible, UV, and X-rays remains beyond the reach of conventional optical components. While various cameras are available for specific wavelength ranges, such as X-ray imaging panels (10–150 keV), silicon-based

PROGRESS AND POTENTIAL

Multi-wavelength imaging is crucial for comprehensive insights into objects, but conventional methods often have limitations such as costly components and restricted wavelength ranges. This work presents stochastic photoluminescence and compressed encoding (SPACE), which utilizes randomly arrayed lanthanide transducers to encode scenes tagged with different excitation wavelengths into a single image that covers X-rays (0.089 nm), ultraviolet (375 nm), and near-infrared I (808 nm) and II (1,532 nm) channels. Expansion to more channels is possible using multi-layer encoders or by controlling the material thickness. This method enables multi-depth visualization and has the potential for multi-spectrum X-ray imaging. Future efforts should focus on enhancing detection efficiency of multi-wavelength imaging sensors. Ultracompact, multi-wavelength imaging sensors hold promise for diverse applications, including wearable microscopes, mobile-phone-integrated cameras, and industrial automation.

imaging sensors (300–1,100 nm), and InGaAs-based NIR detectors (800–1,700 nm), achieving comprehensive imaging from X-ray to NIR involves integrating these three types of cameras. This integration necessitates complex dispersion and connection systems and often entails substantial cost, particularly when incorporating X-ray imagers. Moreover, despite the prevalence of traditional silicon-based imaging sensors with millions of pixels, the creation of compact yet numerous pixels is a challenging task when dealing with special spectral bands such as NIR II and X-rays. Therefore, the pursuit of an all-in-one imaging sensor capable of accommodating multiple wavelengths while maintaining high resolution is a formidable challenge.

Lanthanide materials have recently sparked considerable interest due to their luminescence properties, facilitating light sensitization and emission across a broad spectrum of wavelengths. Moreover, their ability to interact with organic compounds makes them highly versatile as upconversion and downshifting transducers in diverse applications.[10–14] We hypothesize that lanthanide transducers, with readily adjustable narrow excitation and emission bands, substantial Stokes/anti-Stokes shifts, and excellent optical and chemical stability, could serve as wavelength-selective components for multi-wavelength imaging from X-rays to the NIR region.[15–17] In our endeavor to integrate multiple wavelength detection pixels, we have introduced an imaging technique named "stochastic photoluminescence and compressed encoding" (SPACE). This technique involves processing photoluminescence materials into a sparse random array and subsequently combining a compressed sensing (CS) imaging strategy to reconstruct the complete image. By utilizing SPACE, we envision the development of a versatile ultrabroad-band, multi-wavelength compressed imaging sensor. Specifically, stochastic photoluminescence involves the utilization of screen-printed random patterns of luminescent materials that can be excited by light across a wide range of wavelengths. Compressed encoding captures essential multi-wavelength data using a reduced set of measurements, guided by deep learning algorithms.[18–24] This integrated approach enables efficient multi-wavelength, multi-channel imaging by extracting diverse spectral information from a minimal dataset.

RESULTS

As a proof of concept, we selected four lanthanide-doped luminescent materials as transducers. Each transducer converted a specific wavelength, including UV (375 nm), NIR I (808 nm), NIR II (1,532 nm), and X-rays (0.089 nm), into visible light detectable by a common Si-based charge-coupled device (CCD; Figure S1). Each transducer forms a randomly distributed arrays of pixels, with four such arrays complementing each other. Although each array contains the same number of pixels (25% each), their positions are distinct, ultimately forming a complete array. A filter film was used to eliminate the excitation light. They were then integrated with a commercial CCD, constructing an active multi-wavelength-encoded imaging sensor (Figures 1A and 1B). In our multi-wavelength-encoded imaging sensor, each randomly arranged transducer array undersampled the object image and converted its specific wavelength into the visible range. Each type of transducer is randomly distributed and occupies only 25% of the total pixel array of the material layer. Therefore, when an image tagged with a specific wavelength (e.g., 375 nm) is incident on the transducer array, only the image intensity at the pixel positions of the transducers excited by that wavelength can be collected. Consequently, the image of each wavelength channel is only captured by 25% of the pixels, indicating undersampling for each channel. The CS reconstruction algorithm was applied to recover structural information of each wavelength channel from the undersampled

[1]Department of Chemistry, National University of Singapore, Singapore 117543, Singapore

[2]Division of Radiation Oncology, National Cancer Centre Singapore, Singapore, Singapore

[3]Center for Functional Materials, National University of Singapore Suzhou Research Institute, Suzhou 215123, China

[4]Lead contact

*Correspondence: chmlx@nus.edu.sg

https://doi.org/10.1016/j.matt.2024.02.014

Please cite this article in press as: Yi et al., X-ray-to-NIR multi-wavelength imaging through stochastic photoluminescence and compressed encoding, Matter (2024), https://doi.org/10.1016/j.matt.2024.02.014

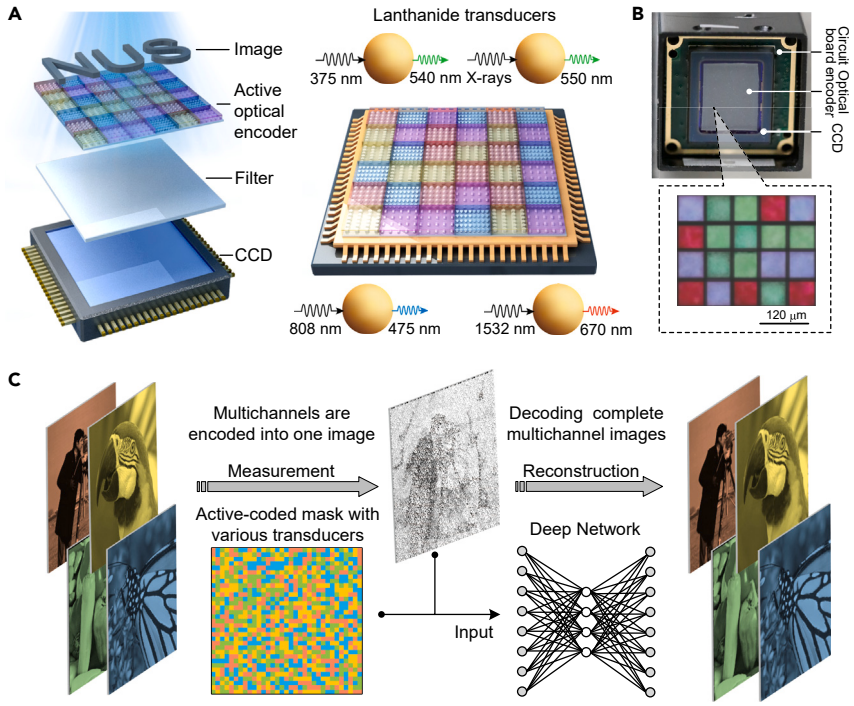

Figure 1. Multi-wavelength imaging sensor through stochastic photoluminescence and compressed encoding (SPACE)

(A) Design of the multi-wavelength imaging sensor based on randomly arrayed lanthanide transducers. Optical encoders, consisting of a variety of lanthanide transducers sensitive to distinct incident wavelengths, encode and convert images acquired through X-rays, UV, and near-infrared light, making them detectable by a charge-coupled device (CCD). A filter is placed under the encoders to remove excitation light.

(B) Photograph of a multi-wavelength imaging sensor fabricated by integrating optical encoders onto a CCD. The inset shows a section of the microscope image of randomly arranged lanthanide-transducer-based optical encoders.

(C) Conceptual scheme of the multi-wavelength imaging, taking four wavelength channels as an example. The four images tagged with four wavelengths are incident on the multi-wavelength imaging sensor simultaneously, and active optical encoders composed of four randomly arrayed transducers encode the four images in different sampling manners and then transmit the luminescence images to the CCD for detection. Finally, the CCD detects one image that is the superimposition of the four encoded images. The encoded images measured by the CCD and the coding mask matrix are fed into a trained deep neural network, which outputs four reconstructed images.

image.[25–30] Instead of directly acquiring the sections of an object tagged with different wavelength, our multi-wavelength-coded imaging sensor acted as a computational pre-processor, encoding and extracting relevant information from the image.[31–33] The computer then works as a post-processor, reconstructing multiple images through a specific algorithm.[34–38]

Specifically, the designed optical encoder, consisting of random arrays of four types of lanthanide transducers, captured four images tagged with different wavelengths. The CCD integrated under the encoder collected the luminescence from the transducers, resulting in a coded image containing the relevant information of the four images (Figure 1C). The designed random patterns of the encoder and the collected encoded images were then fed into a trained end-to-end machine learning reconstruction network,[18,39] generating four complete reconstructed images. Our concept greatly reduces the resolution requirements for the camera while

Please cite this article in press as: Yi et al., X-ray-to-NIR multi-wavelength imaging through stochastic photoluminescence and compressed encoding, Matter (2024), https://doi.org/10.1016/j.matt.2024.02.014

expanding the wavelength coverage of the imaging sensor. In a multi-wavelength-encoded imaging sensor aimed at acquiring C images with distinct wavelengths, each containing N pixels, a camera with N pixels is required. The number of encoding pixels, randomly arranged for each wavelength, is N/C. Subsequently, CS algorithms are applied to reconstruct images for each wavelength with N pixels. In contrast, traditional color cameras employ a regular pattern for filter pixels. Thus, obtaining C images with N pixels for different wavelengths necessitates a camera with $N \times C$ pixels. To obtain images with the same pixel resolution, our multi-wavelength-encoded imaging sensor delivers substantial efficiency, reducing the required number of pixels by a factor of C compared to traditional color cameras (Figure S2). Moreover, the camera's detection extends from X-rays to NIR II wavelengths, enabled by lanthanide transducers.

To demonstrate the feasibility of SPACE for multi-wavelength imaging, we fabricated an active optical encoder using a screen-printing process, consisting of four types of randomly arranged lanthanide transducers with a pixel size of approximately 60 μm (Figures 2A, S3, and S4). Under the excitation of X-rays and specific wavelengths (375, 808, and 1,532 nm), these transducers emitted visible light (Figure 2B). To mitigate the impact of UV radiation on other luminescent materials, the image at 375 nm can be acquired by capturing the afterglow image. We built an imaging system incorporating a light-combining prism group, an adjustable imaging lens group, and a designed multi-wavelength-coded sensor to capture separate images by continuously switching excitation wavelengths (Figure 2C). System parameters used in experiments are described in the Methods section. An image can be represented as a two-dimensional matrix. Stacking the columns of the matrix gives a vector $\boldsymbol{x} \in N^2 \times 1$, where N is the height and width of the image in pixels. For one type of transducer, undersampling an image by an $N \times N$ random array can be mathematically equivalent to linearly multiplying the vector $\boldsymbol{x}$ by a measurement matrix $\boldsymbol{\Phi} \in M \times N2$, where $M/N2$ is the compressed sampling rate. We obtained a vector $\boldsymbol{y}$ with only M pixels. CS reconstruction involves reconstructing the original image $\boldsymbol{x}$ from $\boldsymbol{y}$ and $\boldsymbol{\Phi}$. In our configurations, $\boldsymbol{\Phi}$ is an identity matrix with certain rows removed, resulting in a fat matrix with only one 1 in each row and zeros elsewhere.

To improve reconstruction performance and speed, we employed an end-to-end machine learning algorism instead of traditional iterative-based CS reconstruction algorithms, which are more effective for dense measurement matrices. Specifically, an iterative shrinkage-thresholding algorithm network (ISTA-Net) was used. In this network, all parameters are learned in an end-to-end manner instead of manual configuration (Figure S5).[39] The network takes compressed measurement images corresponding to four wavelengths and the measurement matrix corresponding to the encoder as inputs. Subsequently, it produces four complete reconstructed images (Figure 2D). These reconstructed images accurately depict the content of objects, including onion cells with an approximate size of 200 μm (Figure 2D). The slight blurring of the image tagged with the 375 nm wavelength compared to others is attributed to the smaller size of onion cells (approximately 200 μm), necessitating a higher-resolution imaging system for clearer images. Notably, to reduce the stringent requirements for computer memory, each image was divided into smaller sub-images measuring 100 × 100 pixels. These sub-images were then reconstructed sequentially and stitched together to form the complete image.

Upon analyzing the spatial frequency of reconstructed glass-sphere images (700 × 700 pixels), we observed that all important high-frequency information was reconstructed (Figure 3A). Despite the non-sparse intensity distribution, a majority of

Please cite this article in press as: Yi et al., X-ray-to-NIR multi-wavelength imaging through stochastic photoluminescence and compressed encoding, Matter (2024), https://doi.org/10.1016/j.matt.2024.02.014

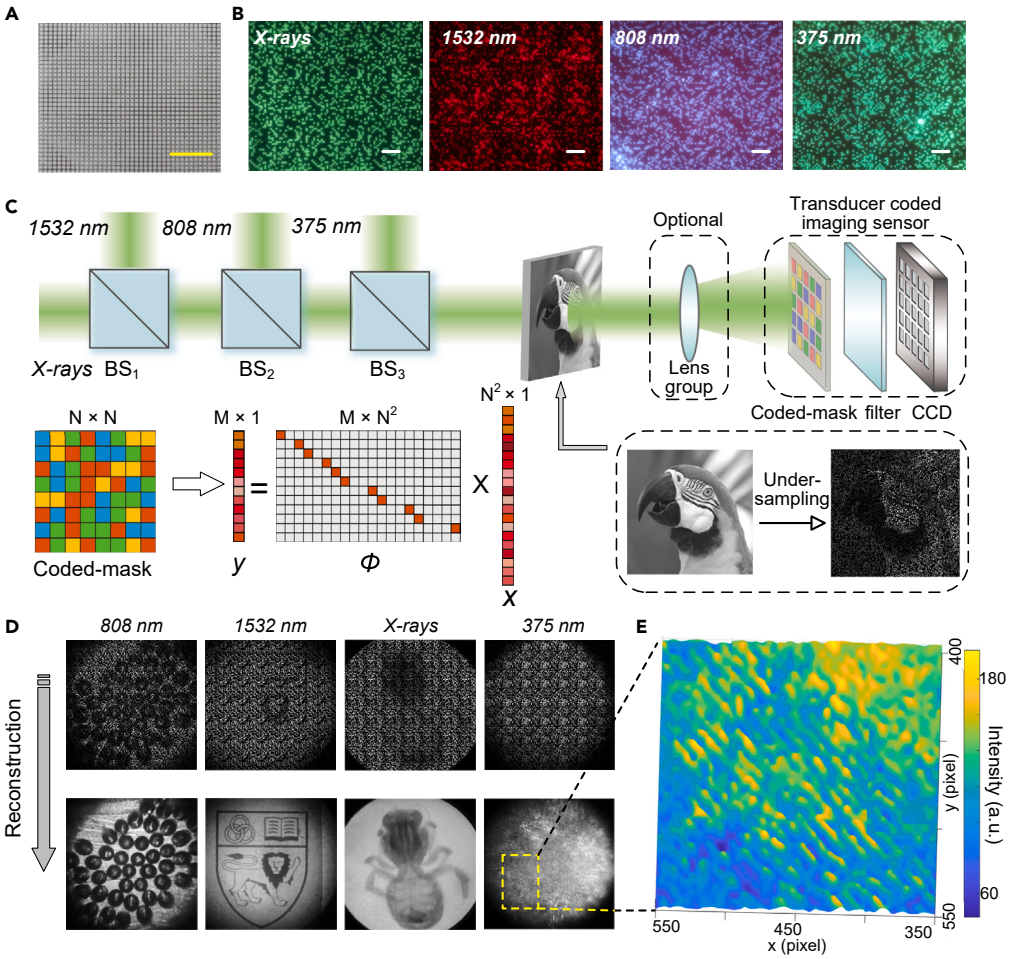

Figure 2. Multi-wavelength imaging with four sets of stochastically printed lanthanide transducers

(A) Microscope image showing a section of optical encoders fabricated with stochastically printed lanthanide transducers (scale bar, 600 μm).

(B) Luminescence photograph of optical encoders excited at various wavelengths (375, 808, and 1,532 nm, and X-rays) with unique random coding schemes.

(C) Schematic of the experimental setup and imaging principle, illustrating the correspondence between different light sources, samples, and lens group adjustments. System parameters used in experiments are described in the Methods section. Images from each wavelength channel are encoded, collected using the multi-wavelength imaging sensor, and processed on a computer. The encoding process involves linear multiplication between the measurement matrix $\boldsymbol{\varphi}$ (encoder representation) and image vector x, resulting in a compressed measurement vector y. Reconstruction of the original image x from y and $\boldsymbol{\varphi}$ is accomplished using a machine learning algorithm.

(D) Imaging results of the four wavelength channels, displaying encoded and reconstructed images.

(E) Zoomed intensity map of the image enclosed within the yellow box in (D).

coefficients in the wavelet domain are zero, indicating the potential for further compression of the glass-sphere image. This was also supported by the results of higher-order wavelet transforms. The low-frequency sub-band (175 × 175 pixels) obtained after applying a level 2 wavelet transform occupies only 1/16 of the original image size. However, it still preserves significant information about the image content. Therefore, it is theoretically possible to extend the wavelength channel further, enabling accurate reconstruction of images compressed at a 10% sampling rate (Figure S6).

It is important to note that the pixel size of the encoder (~60 μm) does not directly represent image resolution because the CCD has a smaller pixel size (<5 μm). To

Please cite this article in press as: Yi et al., X-ray-to-NIR multi-wavelength imaging through stochastic photoluminescence and compressed encoding, Matter (2024), https://doi.org/10.1016/j.matt.2024.02.014

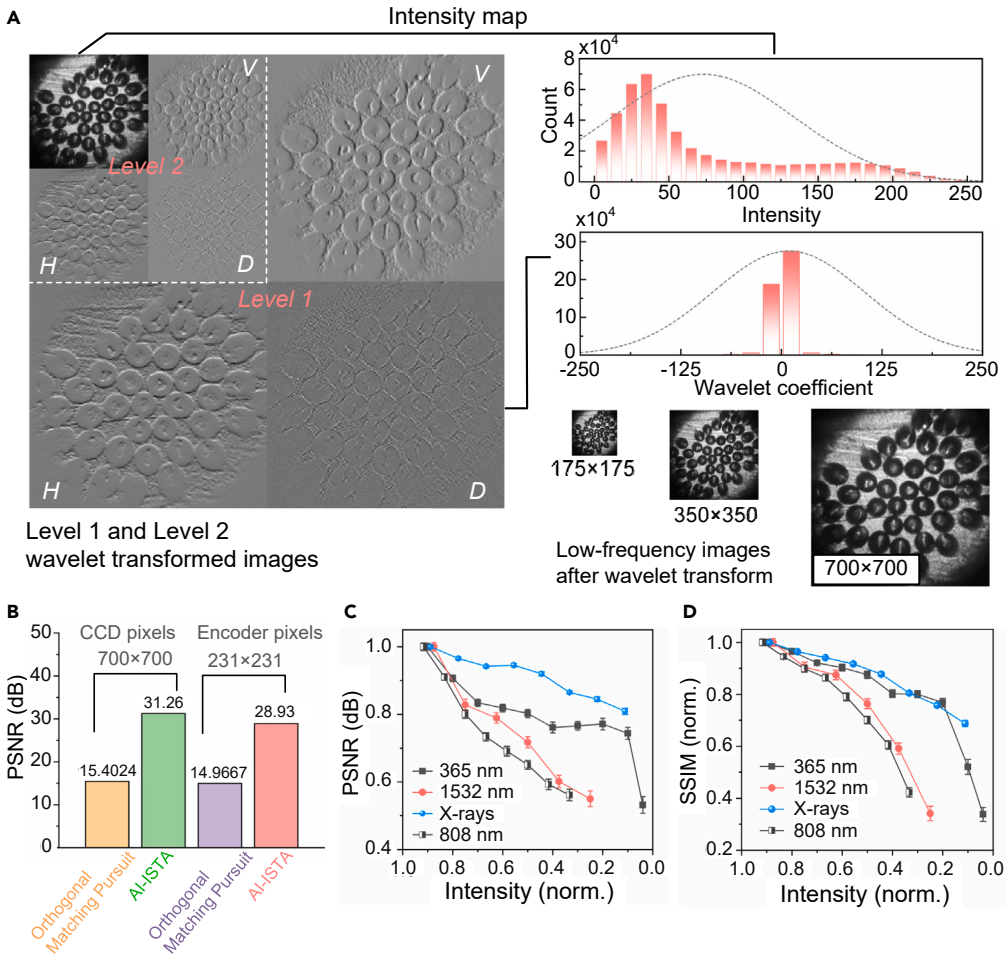

Figure 3. Performance of multi-wavelength imaging through SPACE

(A) Reconstructed glass-sphere image analyzed with level 1 and level 2 wavelet transforms. The wavelet transform divides the input image into low-frequency and high-frequency components using a wavelet function. The high-frequency components are further divided into horizontal (H), vertical (V), and diagonal (D) components through wavelet decomposition. Two histograms illustrate the amplitude distribution in the intensity domain (top) and the wavelet domain (bottom) of the image. The inserted images show the low-frequency components after level 1 and level 2 wavelet transforms of the reconstructed image (700 × 700 pixels), indicating successful compression even at a 1/16 compression rate.

(B) Reconstruction results of the "peppers" image, considering and not considering the multiple CCD pixels covered under each encoder pixel. This includes comparisons between the traditional compressed sensing reconstruction algorithm, orthogonal matching pursuit, and the machine learning reconstruction algorithm ISTA-Net.

(C and D) Peak signal-to-noise ratio (PSNR) and structural similarity index measure (SSIM), respectively, between reconstructed images under different light source powers and the best image. Data are presented as mean values ± SEM, processed from 10 measurements at each power.

demonstrate how image resolution is determined by CCD size, we conducted simulations where the standard image "peppers" (a commonly used test image in the field of image processing; Figure S7) was compressed and reconstructed using different encoding masks and algorithms. Sampling the image at the pixel size of the encoder mask resulted in a reconstructed image of 231 × 231 pixels using ISTA-Net, with a peak signal-to-noise ratio (PSNR) of 28.93 compared to the original image (Figures 3B and S7). In contrast, if we consider that each encoder mask pixel covers 3 × 3 CCD pixels, a higher-resolution image (700 × 700 pixels) can be obtained with an equivalent PSNR of 31.26. Moreover, due to the measurement matrix's insufficient density, the traditional CS reconstruction algorithm (orthogonal matching pursuit) cannot effectively reconstruct the image. The primary factor

Please cite this article in press as: Yi et al., X-ray-to-NIR multi-wavelength imaging through stochastic photoluminescence and compressed encoding, Matter (2024), https://doi.org/10.1016/j.matt.2024.02.014

affecting image reconstruction is the presence of image noise, which largely depends on the light intensity. As the power of the light source gradually decreases, the PSNR and structural similarity index measure (SSIM) of the reconstructed image also decrease compared to the image with the highest quality (Figures 3C and 3D). X-ray images are minimally affected by power, whereas images based on upconversion transducers are more sensitive to power variations. Additionally, under low-light conditions, SSIM tends to decrease more significantly than PSNR. This is because PSNR primarily quantifies the level of noise or distortion between an image and its original version. In contrast, SSIM is a metric used to evaluate the structural similarity between two images, considering various elements such as luminance, noise, and contrast, all of which collectively contribute to its measurement.

A monochrome CCD is sufficient for simultaneously reconstructing four images tagged with four different wavelengths. When combined with a color RGB CCD, lanthanide transducers with varying emission wavelengths allow for the realization of a multi-layer, multi-wavelength-coded imaging sensor, theoretically increasing the number of wavelength channels by 3-fold. To demonstrate this concept, we designed a double-layer optical encoder, with each layer containing two types of randomly arranged lanthanide transducers (Figure 4A). Specifically, the transducers excited by 375 nm radiation emit green light, while those excited by 1,532 nm light emit red light. Both types of transducers are stacked in a random array. Moreover, the transducers excited by 808 nm radiation emit blue light, and those excited by X-rays emit green light. These two types of transducers are also stacked in a random array (Figure 4B). The double-layer encoder captures images from all four wavelength channels but with a sampling ratio of 50%, meaning that the number of pixels for each type of transducer is doubled. A higher sampling rate yields better reconstruction results, but the stacked configuration increases susceptibility to light scattering (Figures 4C and S6). Therefore, the multi-layer, multi-wavelength-coded imaging sensor combined with an RGB CCD is better suited for applications requiring a greater number of wavelength channels.

We next developed a system for multiple-depth imaging by illuminating different parts of a sample with light of varying wavelengths. This approach allows us to simultaneously obtain depth images using multiple wavelengths. As a proof of concept, we constructed an imaging system that utilizes three wavelengths of light to capture images at various depths within the sample, while X-rays are used to acquire interior images (Figure 5A). In the experiment's standard setup, with the image distance set at 200 mm, we find that the focal distances for 375, 808, and 1,532 nm light are 20.4, 21.7, and 22.4 mm, respectively. Each imaging session positions the sample's top surface at the theoretical focal plane corresponding to the 375 nm wavelength. Concurrently, the imaging at 808 and 1,532 nm wavelengths is designed to capture images at depths of 21.7 and 22.4 mm, respectively. When imaging a dragonfly's wings and partial torso, different wavelengths of light can focus on and magnify structures at different depths. However, the torso remains impenetrable to light. Conversely, X-rays can visualize the interior of the torso, but the wing structure lacks clear imaging due to insufficient absorption contrast (Figure 5B). Further, when we raised the sampling rate to 50%, we employed an encoder containing only two materials excited by 375 and 808 nm radiation to capture images of the sample at different depths. The experimental setup and focal depth remain unchanged (Figure 5A). The reconstruction algorithm, based on neural networks, effectively reconstructed images of the two depths (Figure 5C). For example, in the image of a glass sphere, the 375 nm radiation focused and

Please cite this article in press as: Yi et al., X-ray-to-NIR multi-wavelength imaging through stochastic photoluminescence and compressed encoding, Matter (2024), https://doi.org/10.1016/j.matt.2024.02.014

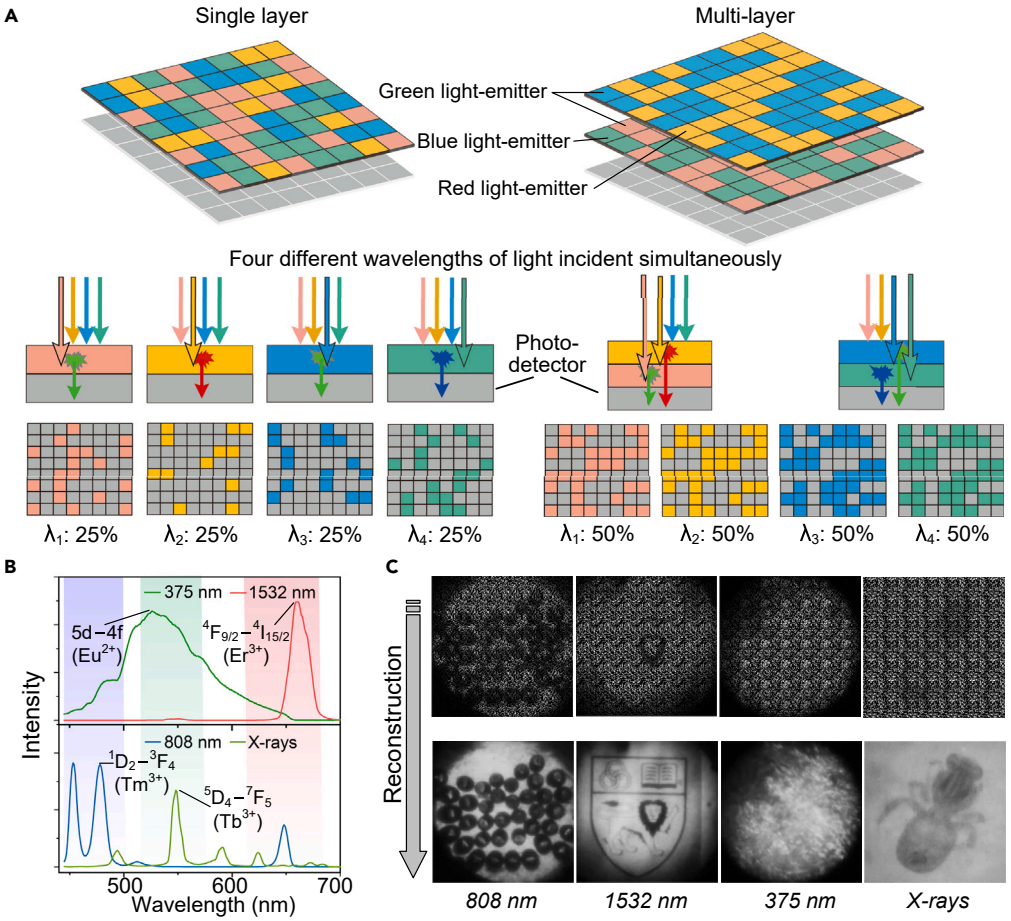

Figure 4. Multi-wavelength imaging using multi-layer optical encoders

(A) Schematic comparison of a single-layer and a double-layer active optical encoder. In the single-layer encoder, four sets of lanthanide transducers are randomly distributed to complement each other, with each CCD pixel covered by only one type of transducer, making a monochrome CCD sufficient. Each transducer array randomly samples the image with a 25% compressed sampling ratio. In the double-layer encoder, each layer contains two types of randomly distributed transducers, with different luminous colors stacked up and down. Each CCD is covered with two types of transducers, necessitating the use of a color RGB CCD. As a result, each transducer captures images with a 50% compressed sampling ratio.

(B) Emission spectra of the four transducer materials under X-ray or 375, 808, or 1,532 nm excitation.

(C) Imaging results of the four wavelength channels, comprising encoded and reconstructed images.

magnified the structure at the sphere's focal plane, while the 808 nm radiation focused and magnified deeper structures.

We also discovered that by controlling the thickness of the scintillator layer, the optical encoder can capture high-energy radiation across multiple wavelengths or energy levels. The photoelectric absorption coefficient of the scintillator exhibits a sharp decrease with increasing photon energy. Consequently, the attenuation thickness differs for KeV X-rays and MeV gamma rays, measuring at sub-millimeter and centimeter levels, respectively (Figure 5D). To explore this, we fabricated an optical encoder comprising randomly arranged pixel arrays with two thicknesses: 200 μm and 2.5 mm. The 200-μm-thick pixel array shows a light output ratio, exceeding 10^5, between X-ray excitation (~15 keV) and gamma-ray excitation (6 MeV). In contrast, the random pixel array with a thickness of 2.5 mm exhibits a light output ratio exceeding 10^5 between gamma-ray excitation and X-ray excitation (Figure 5E). By utilizing a sampling rate of 50%, we reconstructed the X-ray

Please cite this article in press as: Yi et al., X-ray-to-NIR multi-wavelength imaging through stochastic photoluminescence and compressed encoding, Matter (2024), https://doi.org/10.1016/j.matt.2024.02.014

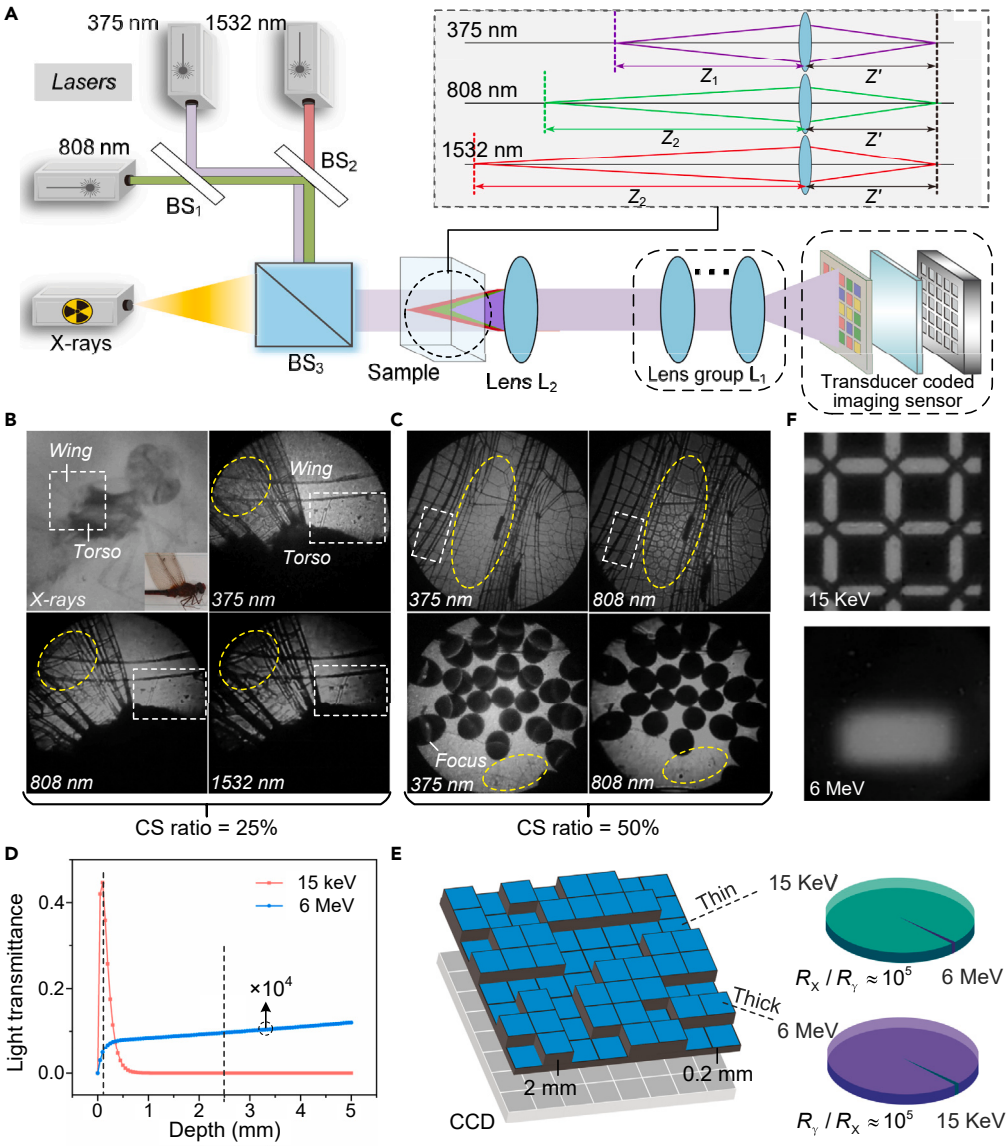

Figure 5. Multi-wavelength and multi-depth imaging by controlling the thickness of the optical encode layer

(A) Schematic diagram of the experimental setup for multi-channel imaging. An aberration lens L_1 collects light of various wavelengths at different sample depths, which is then transmitted to the detector. X-rays, capable of penetrating the entire sample, are also sent to the detector. System parameters used in experiments are described in the Methods section.

(B) Reconstructed images of dragonfly wings and partial torso simultaneously imaged at four wavelengths, with a compression ratio of 25% for each wavelength channel. The white and yellow dotted boxes mark the typical complementary structural information obtained from different channel images.

(C) Reconstructed images of dragonfly wings and glass spheres simultaneously imaged at 375 and 808 nm, with a compression ratio of 50% for each wavelength channel. The white and yellow dotted boxes mark the typical complementary structural information obtained from different channel images. For example, the 375 nm wavelength image focuses and magnifies the structure at the focal plane of the sphere, while the 808 nm wavelength image focuses and magnifies the deeper structure.

(D) Calculated light output of scintillator layers with different thicknesses under X-ray (~15 keV) and gamma-ray (6 MeV) irradiation.

(E) Optical encoder specifically designed for imaging both X-rays (pixel thickness: ~200 μm) and gamma rays (pixel thickness: ~2.5 mm). In thin pixels, the ratio between X-ray and gamma-ray radioluminescence output is approximately 10^5. Similarly, in thick pixels, the ratio of gamma-ray to X-ray radioluminescence output is approximately 10^5.

(F) Reconstructed images of a stencil under X-rays and spot shape under gamma rays, with a compression ratio of 50% for each channel.

Please cite this article in press as: Yi et al., X-ray-to-NIR multi-wavelength imaging through stochastic photoluminescence and compressed encoding, Matter (2024), https://doi.org/10.1016/j.matt.2024.02.014

image of a stencil and the gamma-ray beam shape from medical radiotherapy equipment (Figure 5F).

DISCUSSION

In conclusion, our utilization of SPACE presents a solution to overcome the constraints of existing multi-wavelength imaging technologies. Our active multi-wavelength-coded imaging sensor, which incorporates randomly arrayed lanthanide transducers and a CS deep learning reconstruction algorithm, enables high-quality simultaneous imaging across a broad spectrum of wavelengths. This approach reduces camera resolution requirements and simplifies electronic post-processing. The combination of active optical encoders and CS not only allows for imaging with fewer pixels but also results in lower photon counts, higher throughput, and reduced latency. The SPACE approach is also applicable to various multi-channel imaging techniques, such as multi-lifetime, multi-polarization, and multi-phase imaging,[40] with potential use in fields like biomedical imaging, food and agriculture, materials science, and geological and mining exploration, among others.

The image captured with 375 nm light relies on the residual luminescence emitted by transducers, as other materials also respond to this excitation. This demonstration highlights a key advantage of using transducer materials in multi-wavelength imaging as encoders: the ability to utilize the different luminescence lifetimes of materials to expand the number of wavelength channels available. However, for high-dynamic-range imaging, it would be ideal to use transducer materials that exhibit entirely distinct luminescence emissions under different excitations. In addition, it is important to acknowledge that our current detection sensitivity, as proven through a random array of lanthanide-doped transducers at high concentrations, allows imaging using conventional visible light cameras at an approximate power of 15 mW/cm^2. Nevertheless, this level of sensitivity may not support multi-wavelength imaging under extremely low-light conditions due to the limited efficiency of the luminescent materials used. Future work should focus on enhancing detection efficiency in three key areas: improving luminescent efficiency through materials engineering, employing more efficient energy conversion systems, and leveraging optical engineering techniques to compensate for material limitations.[41] Moreover, the efficiency of photodetectors can be further enhanced with the use of high-quality image sensors featuring low electronic noise. Despite the existing limitations, the development of ultracompact, multi-wavelength imaging sensors opens possibilities for advanced imaging applications and holds the potential for advancements across diverse sectors, including wearable microscopes, mobile-phone-integrated hyperspectral cameras, and industrial automation.

EXPERIMENTAL PROCEDURES

Resource availability

Lead contact

Further information and requests for resources should be directed to and will be fulfilled by the lead contact, Professor Xiaogang Liu (chmlx@nus.edu.sg).

Materials availability

$Gd_2O_2S:Tb^{3+}$ and $SrAl_2O_4:Eu^{2+}/Dy^{3+}$ phosphors were purchased from Xiucai Chemical (Foshan, China). $NaYbF_4:Yb^{3+}/Er^{3+}$ phosphors were purchased from Zhanwanglong Technology (Shenzhen, China). $NaYF_4:Yb^{3+}/Tm^{3+}@NaYF_4:Yb^{3+}/Nd^{3+}$ phosphors were synthesized according to the method described in the literature, with some modifications[42] (Figure S1).

Please cite this article in press as: Yi et al., X-ray-to-NIR multi-wavelength imaging through stochastic photoluminescence and compressed encoding, Matter (2024), https://doi.org/10.1016/j.matt.2024.02.014

Data and code availability

All relevant data that support the findings of this work are available from the corresponding author upon reasonable request.

Characterizations

$Gd_2O_2S:Tb^{3+}$, a gadolinium oxalate crystal doped with Tb^{3+} ions, emits green light when exposed to X-rays. The luminescence mechanism is based on the absorption of X-ray energy by Gd^{3+} ions, causing internal electrons to transition from the ground state to excited states. Energy transfer then occurs from the excited Gd^{3+} ions to Tb^{3+} ions, leading to radiative transitions of the excited Tb^{3+} ions back to their ground state. Photons are released during this process, and the transition between the $^5D_4$ and ^7F_J (J = 6, 5, 4, 3) energy levels of Tb^{3+} ions produces visible light at about 489, 543, 586, and 619 nm.[43,44] This material emits a bright green color when excited by X-rays.

When $NaYbF_4:Yb^{3+}/Er^{3+}$ transducers are excited with 1,532 nm radiation, the Er^{3+} ions absorb the photons and transition to a higher energy state. Subsequently, the excited Er^{3+} ions transfer energy to neighboring Yb^{3+} ions or Er^{3+} ions, promoting them to an excited state. Next, the excited Yb^{3+} or Er^{3+} ions transfer energy to other ground-state Er^{3+} ions, facilitating their transition to even higher energy states. Finally, the excited Er^{3+} ions return to their ground state through radiative transition, emitting red at approximately 660 nm.[45,46]

$NaYF_4$:Yb/Tm@$NaYF_4$:Yb/Nd transducers emit blue light under 808 nm excitation. The luminescence mechanism involves the absorption of 808 nm photons by Nd^{3+} ions, which then transfer energy to neighboring Yb^{3+} ions, promoting them to an excited state. The excited Yb^{3+} ions further transfer energy to Tm^{3+} ions, possibly by multiple energy transfer, resulting in highly excited Tm^{3+} ions. These excited Tm^{3+} ions then return to their ground state through radiative transition between the $^1D_2$ and $^3F_4$ energy levels of Tm^{3+} ions, generating blue light at approximately 475 nm.

The luminescence of $SrAl_2O_4:Eu^{2+}/Dy^{3+}$ transducers is likely governed by an electron-trapping mechanism.[47] This mechanism involves the excitation of Eu^{2+}'s 5d electron to the host's conduction band, resulting in the generation of Eu^{3+} and the capture of this electron by Dy^{3+}, causing its reduction to Dy^{2+}. In this context, the trapped electron can be thermally released and subsequently recombine with Eu^{3+} to produce delayed luminescence. At room temperature, the emission spectrum shows a characteristic broad band centered at 520 nm attributed to Eu^{2+}, corresponding to the electric-dipole-allowed 4f-5d transition.

Methods

Fundamental principle of SPACE

To illustrate the process of how a luminescent material array samples an intensity image, we can use an example of a specific wavelength channel, such as the $SrAl_2O_4:Eu^{2+}/Dy^{3+}$ material array responding to 375 nm. The complete intensity image with $N \times N$ pixels encoded with the 375 nm radiation can be represented by a two-dimensional matrix $\mathbf{I} \in N \times N$. When the intensity image is incident on the randomly arranged luminescent material array, the array samples the image in a random and undersampled manner. This sampling process can be described by a sampling matrix $\boldsymbol{\varphi}$, which represents the locations of the luminescent materials in the array. The image collected by the CCD is the result of linear multiplication of the complete intensity image $\mathbf{I}$ and the measurement matrix $\boldsymbol{\varphi}$, which represents

Please cite this article in press as: Yi et al., X-ray-to-NIR multi-wavelength imaging through stochastic photoluminescence and compressed encoding, Matter (2024), https://doi.org/10.1016/j.matt.2024.02.014

the sampling process of the luminescent material array. This process can be described as a matrix equation:

$$\mathbf{H} = \mathbf{I} \cdot \boldsymbol{\varphi}, \quad \text{(Equation 1)}$$

where $\mathbf{H}$ is the measured image by CCD.

In the array of luminescent materials, the pixels that do not respond to the 375 nm excitation light do not emit light. Therefore, the measurement matrix $\boldsymbol{\varphi}$ has a value of 0 at those positions and 1 at the pixel positions that respond to the 375 nm excitation. If the $N \times N$ pixels in the intensity image are equally divided into four wavelength channels, then the number of pixels with a value of 1 in the measurement matrix $\boldsymbol{\varphi}$ is $M = N^2/4$ (Figure S3). This means that in the image $\mathbf{H}$ measured by the CCD, only M pixels are useful and contain the image information, while the other values are all 0 and can be removed. By removing the redundant 0 values, we can effectively reduce the size of the image and improve the efficiency of image processing.

In practice, a large number of images need to be processed. To simplify the calculations, the image matrix $\mathbf{I}$ is treated as a vector $\boldsymbol{x} \in N^2 \times 1$ by stacking the columns of the matrix $\mathbf{I}$. The measurement matrix $\boldsymbol{\varphi}$ is transformed into $\boldsymbol{\xi} \in M \times N^2$, where each row has only one pixel with a value of 1 and the others are all 0. Accordingly, the image $\mathbf{H}$ collected by the CCD can be represented as a vector $\boldsymbol{y} \in M \times 1$ and expressed as

$$\boldsymbol{y} = \boldsymbol{\xi} \cdot \boldsymbol{x} + e, \quad \text{(Equation 2)}$$

where e is the noise. The objective of various CS reconstruction algorithms is to solve for complete image $\boldsymbol{x}$ in terms of $\boldsymbol{y}$ and $\boldsymbol{\xi}$.

ISTA-Net

Given the measurements $\boldsymbol{y}$, the traditional CS reconstruction algorisms usually reconstruct the original image $\boldsymbol{x}$ by solving the following (generally convex) optimization problem:

$$\min_x \frac{1}{2}\|\boldsymbol{\xi}x - y\|_2^2 + \lambda\|\boldsymbol{\psi}x\|_1. \quad \text{(Equation 3)}$$

Here, $\boldsymbol{\Psi}x$ denotes the transform coefficients of $\boldsymbol{x}$ with respect to some transform $\boldsymbol{\Psi}$, and the sparsity of the vector $\boldsymbol{\Psi}x$ is promoted by the ℓ_1 norm. λ is a generally predefined regularization parameter that controls the trade-off between the sparsity of $\boldsymbol{\Psi}x$ and the fidelity of the reconstructed image.

The ISTA is a first-order proximal method that solves the CS reconstruction problem in Equation 3 by iterating between the following update steps:

$$r^{(k)} = x^{(k-1)} - \rho\boldsymbol{\xi}^{\mathrm{T}}\left(\boldsymbol{\xi}x^{(k-1)} - y\right) \quad \text{(Equation 4)}$$

$$x^{(k)} = \operatorname*{argmin}_x \frac{1}{2}\left\|x - r^{(k)}\right\|_2^2 + \lambda\|\boldsymbol{\psi}x\|_1. \quad \text{(Equation 5)}$$

Here, k denotes the ISTA iteration index and ρ is the step size (Figure S5).

The choice of a sparse transformation $\boldsymbol{\Psi}$ plays a critical role in the performance of the CS reconstruction. The commonly used transforms include the wavelet transform, the discrete cosine transform, and the Fourier transform. In the ISTA-Net approach, a general non-linear transform function was used to sparsify natural images, denoted by $H(\cdot)$, with learnable parameters. $H(\cdot)$ was designed as a combination of two linear

Please cite this article in press as: Yi et al., X-ray-to-NIR multi-wavelength imaging through stochastic photoluminescence and compressed encoding, Matter (2024), https://doi.org/10.1016/j.matt.2024.02.014

convolution operators (without bias terms) separated by a rectified linear unit. By replacing Ψ in Equation 5 with $H(\cdot)$, it becomes

$$x^{(k)} = \underset{x}{\operatorname{argmin}} \frac{1}{2}\|x - r^{(k)}\|_2^2 + \lambda\|H(x)\|_1. \quad \text{(Equation 6)}$$

$x^{(k)}$ can be efficiently computed in closed form as

$$x^{(k)} = \tilde{H}\left(soft\left(H\left(r^{(k)}, \theta\right)\right)\right), \quad \text{(Equation 7)}$$

where $\theta = \lambda\alpha$; α is a scalar that is only related to the parameters of $H(\cdot)$. θ, as a shrinkage threshold, is a learnable parameter. $\tilde{H}(\cdot)$ is designed to exhibit a structure symmetrical to $H(\cdot)$.

Each module in each phase of ISTA-Net corresponds to the update steps in an ISTA iteration. The learnable parameter set in ISTA-Net consists of the step size $\rho^{(k)}$ in the $r^{(k)}$ module, the parameters of the forward and backward transforms $H(\cdot)$, and the shrinkage threshold θ(k) in the x(k) module.

The end-to-end loss function for ISTA-Net is as follows:

$$L = \frac{1}{N_b N}\sum_{i=1}^{N_b}\left\|x_i^{(N_p)} - x_i\right\|_2^2 + \gamma\frac{1}{N_b N}\sum_{i=1}^{N_b}\sum_{k=1}^{N_p}\left\|\tilde{H}^{(k)}\left(H^{(k)}(x_i)\right) - x_i\right\|_2^2, \quad \text{(Equation 8)}$$

where N_p, N_b, N, and γ are the total number of ISTA-Net phases, the total number of training blocks, the size of each block x_i, and the regularization parameter, respectively.

Configurations of all algorithms

We began by downloading the T91 Image Dataset from the Kaggle platform, which consists of 91 images. Each image was enlarged by a factor of 3 and then cropped into approximately 60,000 sub-images with a pixel size of 100 × 100. Adjacent sub-images have an overlap of 75 pixels. These 60,000 sub-images were used as the training dataset for ISTA-Net. ISTA-Net was implemented in Python 3.7 using Tensorflow 1.13.1 as the operating environment and Pycharm as the integrated development environment. All experiments were conducted on a workstation equipped with an E5-2680V3 CPU and an RTX 2080 Ti GPU. The standard dataset Set11 was used for testing, which contains 11 grayscale images with multi-wavelength channels. The orthogonal matching pursuit algorithm was compiled using MATLAB2020a.

Training and reconstruction process

Specific training steps involve generating a corresponding measurement matrix φ based on the given compressive sensing ratio and the designed pattern of a randomly distributed encoding matrix. The size of the matrix φ is $M \times N$, where $N = 10{,}000$, meaning that each sub-image has a size of 100 × 100. $M = C \times N$, where C represents the compression ratio. Applying $y = \varphi x$ produces a set of CS measurements, where x is the vectorized version of sub-image blocks. The original image x and the corresponding sparse measurement data y constitute the training dataset. The network architecture used and the definition of the loss function are described in the section ISTA-Net. The training dataset, i.e., the original image x and sparse measurement data y, are provided as inputs to the neural network. The network maps the y to a reconstructed image $\tilde{x}$ through forward propagation. The network employs a loss function to evaluate the quality of the reconstructed image $\tilde{x}$ compared with x and utilizes the backpropagation algorithm to compute gradients.

Please cite this article in press as: Yi et al., X-ray-to-NIR multi-wavelength imaging through stochastic photoluminescence and compressed encoding, Matter (2024), https://doi.org/10.1016/j.matt.2024.02.014

Subsequently, the network's weights and biases are updated using the gradient descent to minimize the loss function. These steps are repeated iteratively to train the neural network, with a training duration of 100 epochs. Once the training is complete, we can use the trained neural network to perform compressive sensing reconstruction on new measurement data y, generating high-quality reconstructed images $\tilde{x}$. Unlike random initialization of $\tilde{x}$, a linear mapping matrix is used here, which is learned from training data pairs of CS measurement data and the corresponding image blocks. This matrix is then employed to compute the initial estimate of the image for the compressive sensing reconstruction process.

Fabrication of multi-wavelength compressed imaging sensors

Screen printing is a widely employed printing method to transfer intricate designs onto various substrates, including textiles, ceramics, glass, and other materials. First, the stencil is designed with a random hole array for every wavelength channel. Using computer-aided design software, four different digital stencils are created for four different materials. The stencils are fabricated using a precise laser cutting process and have a thickness of 30 μm. Then, a flat glass substrate coated with transparent, high-quality double-sided adhesive is used as a processing base (Figure S4). The stencil is carefully positioned on the glass substrate to ensure proper alignment. Subsequently, a uniform layer of 100% powder is evenly spread onto the stencil. The powder is then pressed firmly to fill the template pattern and adhere to the double-sided tape on the glass substrate. Following the purging of the template with nitrogen to remove any loose powder residue, the stencil is gently removed.

After screen printing a single array of optical materials onto a glass substrate coated with double-sided tape, the process was repeated to create the second, third, and fourth arrays of optical materials, each designed to respond to different wavelengths. To ensure proper alignment of subsequent arrays, the layer deposited on the glass substrate is placed on the mask holder of a mask aligner (URE-2000/17). The arrays are manually aligned using the x, y, and tilt axes. The aligned array is then pressed to ensure that the plane is flat, and finally, the sample is removed from the aligner. A 200-mm-thick layer of PDMS is applied to the sample and heated to 60°C after vacuuming. Once solidified, the PDMS, featuring four imprinted patterns, is peeled off from the glass substrate, resulting in an approximately powder-to-PDMS ratio of 4:1 in each pixel.

Typical imaging system parameters used in experiments

In the system depicted in Figure 2, samples imaged at each wavelength are captured separately. The light-combining group consists of three broadband beam splitters (BSW29, Thorlabs). The lens system comprises a Nikon Plan Fluor 10× microscope objective and a Canon EF 100 mm f/2.8 macro lens, with approximately 25 cm spacing between the two lens groups. These are followed by the designed imaging sensor. The lenses are removed during X-ray imaging.

In the imaging system depicted in Figure 4, the light-combining group consists of three broadband beam splitters (BSW29, Thorlabs). The imaging portion comprises an objective lens L_1 and imaging lenses L_2. The specific number of lenses, their parameters, and axial chromatic aberration should be determined based on the required magnification, resolution, and imaging performance depending on the actual application needs. In the typical experimental setup used for demonstration, we designed an imaging system with an overall magnification factor of ~4 (magnification varies for different wavelengths). This system includes an imaging objective lens L_1 with a numerical aperture of approximately 0.2, and lens L_2 is a

concave-convex lens with a focal length of approximately 200 mm (the focal length varies for different wavelengths). The distance between the lenses is approximately 135 mm. The object is placed at approximately 20 mm from the objective lens. The light of different wavelengths converges and magnifies the object at different depths.

Calculated light output of scintillator layers

The photoelectric absorption coefficient α in cm^2/g for the GOS:Tb scintillator at different X-ray energy levels was obtained from the database.[47] The density ρ of GOS:Tb is expressed in units of g/cm^3, so the absorption rate of GOS:Tb can be expressed as $\alpha\rho$, measured in cm^{-1}. The attenuation coefficient for the visible light generated is denoted as μ in units of cm^{-1}. Assuming the total thickness of the scintillator is h, the intensity of visible light produced by the scintillator at depth z and transmitted to the bottom surface of the scintillator can be described as follows:

$$I = I_0\{\exp[-\alpha\rho(z - dz)] - \exp(-\alpha\rho z)\}\exp[-\mu(h - z)], \quad \text{(Equation 9)}$$

where I_0 is the initial intensity of X-rays. Therefore, for different thicknesses h, the overall light transmittance is calculated as

$$T = \int_0^h \frac{I}{I_0} dz. \quad \text{(Equation 10)}$$

It should be noted that the above calculations assume that all absorbed X-ray photons are entirely converted into visible light photons.

SUPPLEMENTAL INFORMATION

Supplemental information can be found online at https://doi.org/10.1016/j.matt.2024.02.014.

ACKNOWLEDGMENTS

This work was supported by the National Research Foundation, Prime Minister's Office, Singapore, under its Competitive Research Program (award no. NRF-CRP23-2019-0002) and under its NRF Investigatorship Programme (award no. NRF-NRFI05-2019-0003), as well as the RIE2025 Manufacturing, Trade and Connectivity (MTC) Programmatic Fund (award no. M21J9b0085).

AUTHOR CONTRIBUTIONS

L.Y., B.H., and X.L. conceived and designed the project. X.L. supervised the project. L.Y. built the theoretical model, designed the experiment, and processed image data. B.H. performed microdevice fabrication. B.H., L.Y., and H.Q.T. performed gamma-ray experiments. L.Y. and B.H. wrote the manuscript. X.L. edited the manuscript. All authors participated in the discussion and analysis of the manuscript.

DECLARATION OF INTERESTS

The authors declare no competing interests.

Received: January 31, 2024
Revised: February 11, 2024
Accepted: February 20, 2024
Published: March 13, 2024

REFERENCES

1. Gut, G., Herrmann, M.D., and Pelkmans, L. (2018). Multiplexed protein maps link subcellular organization to cellular states. Science *361*, eaar7042.
2. Tian, L., Yang, Y., Wysocki, L.M., Arnold, A.C., Hu, A., Ravichandran, B., Sternson, S.M., Looger, L.L., and Lavis, L.D. (2012). Selective esterase-ester pair for targeting small molecules with cellular specificity. Proc. Natl. Acad. Sci. USA *109*, 4756–4761.
3. Chia, Y.H., Yeh, J.A., Huang, Y.Y., and Luo, Y. (2020). Simultaneous multi-color optical sectioning fluorescence microscopy with wavelength-coded volume holographic gratings. Opt Express *28*, 37177–37187.
4. Cutrale, F., Trivedi, V., Trinh, L.A., Chiu, C.L., Choi, J.M., Artiga, M.S., and Fraser, S.E. (2017). Hyperspectral phasor analysis enables multiplexed 5D in vivo imaging. Nat. Methods *14*, 149–152.
5. Valm, A.M., Cohen, S., Legant, W.R., Melunis, J., Hershberg, U., Wait, E., Cohen, A.R., Davidson, M.W., Betzig, E., and Lippincott-Schwartz, J. (2017). Applying systems-level spectral imaging and analysis to reveal the organelle interactome. Nature *546*, 162–167.
6. Hua, X., Wang, Y., Wang, S., Zou, X., Zhou, Y., Li, L., Yan, F., Cao, X., Xiao, S., Tsai, D.P., et al. (2022). Ultra-compact snapshot spectral light-field imaging. Nat. Commun. *13*, 2732.
7. Tan, S., Yang, F., Boominathan, V., Veeraraghavan, A., and Naik, G.V. (2021). 3D imaging using extreme dispersion in optical metasurfaces. ACS Photonics *8*, 1421–1429.
8. Yako, M., Yamaoka, Y., Kiyohara, T., Hosokawa, C., Noda, A., Tack, K., Spooren, N., Hirasawa, T., and Ishikawa, A. (2023). Video-rate hyperspectral camera based on a CMOS-compatible random array of Fabry–Pérot filters. Nat. Photonics *17*, 218–223.
9. Pian, Q., Yao, R., Sinsuebphon, N., and Intes, X. (2017). Compressive hyperspectral time-resolved wide-field fluorescence lifetime imaging. Nat. Photonics *11*, 411–414.
10. Wegh, R.T., Donker, H., Oskam, K.D., and Meijerink, A. (1999). Visible quantum cutting in $LiGdF_4$: Eu^{3+} through downconversion. Science *283*, 663–666.
11. Lee, C., Xu, E.Z., Liu, Y., Teitelboim, A., Yao, K., Fernandez-Bravo, A., Kotulska, A.M., Nam, S.H., Suh, Y.D., Bednarkiewicz, A., et al. (2021). Giant nonlinear optical responses from photon-avalanching nanoparticles. Nature *589*, 230–235.
12. Chen, G., Yang, C., and Prasad, P.N. (2013). Nanophotonics and nanochemistry: controlling the excitation dynamics for frequency up-and down-conversion in lanthanide-doped nanoparticles. Acc. Chem. Res. *46*, 1474–1486.
13. Zhou, J., Liu, Q., Feng, W., Sun, Y., and Li, F. (2015). Upconversion luminescent materials: advances and applications. Chem. Rev. *115*, 395–465.
14. Li, S., Zhou, L., and Zhang, H. (2022). Investigation progresses of rare earth complexes as emitters or sensitizers in organic light-emitting diodes. Light Sci. Appl. *11*, 177.
15. Rocha, J., Carlos, L.D., Paz, F.A.A., and Ananias, D. (2011). Luminescent multifunctional lanthanides-based metal–organic frameworks. Chem. Soc. Rev. *40*, 926–940.
16. Ou, X., Qin, X., Huang, B., Zan, J., Wu, Q., Hong, Z., Xie, L., Bian, H., Yi, Z., Chen, X., et al. (2021). High-resolution X-ray luminescence extension imaging. Nature *590*, 410–415.
17. Liu, Y., Lu, Y., Yang, X., Zheng, X., Wen, S., Wang, F., Vidal, X., Zhao, J., Liu, D., Zhou, Z., et al. (2017). Amplified stimulated emission in upconversion nanoparticles for super-resolution nanoscopy. Nature *543*, 229–233.
18. Huang, L., Luo, R., Liu, X., and Hao, X. (2022). Spectral imaging with deep learning. Light Sci. Appl. *11*, 61.
19. Chen, C., Chen, J., Han, H., Chao, L., Hu, J., Niu, T., Dong, H., Yang, S., Xia, Y., Chen, Y., and Huang, W. (2022). Perovskite solar cells based on screen-printed thin films. Nature *612*, 266–271.
20. Pégard, N.C., Liu, H.Y., Antipa, N., Gerlock, M., Adesnik, H., and Waller, L. (2016). Compressive light-field microscopy for 3D neural activity recording. Optica *3*, 517–524.
21. Szameit, A., Shechtman, Y., Osherovich, E., Bullkich, E., Sidorenko, P., Dana, H., Steiner, S., Kley, E.B., Gazit, S., Cohen-Hyams, T., et al. (2012). Sparsity-based single-shot subwavelength coherent diffractive imaging. Nat. Mater. *11*, 455–459.
22. Sun, M.J., Edgar, M.P., Gibson, G.M., Sun, B., Radwell, N., Lamb, R., and Padgett, M.J. (2016). Single-pixel three-dimensional imaging with time-based depth resolution. Nat. Commun. *7*, 12010.
23. Liang, J., Wang, P., Zhu, L., and Wang, L.V. (2020). Single-shot stereo-polarimetric compressed ultrafast photography for light-speed observation of high-dimensional optical transients with picosecond resolution. Nat. Commun. *11*, 5252.
24. Zhu, L., Zhang, W., Elnatan, D., and Huang, B. (2012). Faster STORM using compressed sensing. Nat. Methods *9*, 721–723.
25. Gao, L., Liang, J., Li, C., and Wang, L.V. (2014). Single-shot compressed ultrafast photography at one hundred billion frames per second. Nature *516*, 74–77.
26. Edgar, M.P., Gibson, G.M., and Padgett, M.J. (2018). Principles and prospects for single-pixel imaging. Nat. Photonics *13*, 13–20.
27. Miao, J., Ercius, P., and Billinge, S.J.L. (2016). Atomic electron tomography: 3D structures without crystals. Science *353*, aaf2157.
28. Nicoletti, O., de la Peña, F., Leary, R.K., Holland, D.J., Ducati, C., and Midgley, P.A. (2013). Three-dimensional imaging of localized surface plasmon resonances of metal nanoparticles. Nature *502*, 80–84.
29. Arai, K., Belthangady, C., Zhang, H., Bar-Gill, N., DeVience, S.J., Cappellaro, P., Yacoby, A., and Walsworth, R.L. (2015). Fourier magnetic imaging with nanoscale resolution and compressed sensing speed-up using electronic spins in diamond. Nat. Nanotechnol. *10*, 859–864.
30. Goris, B., Bals, S., Van den Broek, W., Carbó-Argibay, E., Gómez-Graña, S., Liz-Marzán, L.M., and Van Tendeloo, G. (2012). Atomic-scale determination of surface facets in gold nanorods. Nat. Mater. *11*, 930–935.
31. Yuan, S., Ma, C., Fetaya, E., Mueller, T., Naveh, D., Zhang, F., and Xia, F. (2023). Geometric deep optical sensing. Science *379*, eade1220.
32. Altmann, Y., McLaughlin, S., Padgett, M.J., Goyal, V.K., Hero, A.O., and Faccio, D. (2018). Quantum-inspired computational imaging. Science *361*, eaat2298.
33. Hunt, J., Driscoll, T., Mrozack, A., Lipworth, G., Reynolds, M., Brady, D., and Smith, D.R. (2013). Metamaterial apertures for computational imaging. Science *339*, 310–313.
34. Watts, C.M., Shrekenhamer, D., Montoya, J., Lipworth, G., Hunt, J., Sleasman, T., Krishna, S., Smith, D.R., and Padilla, W.J. (2014). Terahertz compressive imaging with metamaterial spatial light modulators. Nat. Photonics *8*, 605–609.
35. Pascucci, M., Ganesan, S., Tripathi, A., Katz, O., Emiliani, V., and Guillon, M. (2019). Compressive three-dimensional super-resolution microscopy with speckle-saturated fluorescence excitation. Nat. Commun. *10*, 1327.
36. Wu, D., Luo, J., Huang, G., Feng, Y., Feng, X., Zhang, R., Shen, Y., and Li, Z. (2021). Imaging biological tissue with high-throughput single-pixel compressive holography. Nat. Commun. *12*, 4712.
37. Chen, S.C., Feng, Z., Li, J., Tan, W., Du, L.H., Cai, J., Ma, Y., He, K., Ding, H., Zhai, Z.H., et al. (2020). Ghost spintronic THz-emitter-array microscope. Light Sci. Appl. *9*, 99.
38. Ota, S., Horisaki, R., Kawamura, Y., Ugawa, M., Sato, I., Hashimoto, K., Kamesawa, R., Setoyama, K., Yamaguchi, S., Fujiu, K., et al. (2018). Ghost cytometry. Science *360*, 1246–1251.
39. Zhang, J., and Ghanem, B. (2018). IEEE Conference on Computer Vision and Pattern Recognition, pp. 1828–1837.
40. Xiong, B., Liu, Y., Xu, Y., Deng, L., Chen, C.W., Wang, J.N., Peng, R., Lai, Y., Liu, Y., and Wang, M. (2023). Breaking the limitation of polarization multiplexing in optical metasurfaces with engineered noise. Science *379*, 294–299.
41. Kim, J.H., and Kim, J.H. (2012). Encapsulated triplet-triplet annihilation-based upconversion in the aqueous phase for sub-band-gap semiconductor photocatalysis. J. Am. Chem. Soc. *134*, 17478–17481.
42. Xie, X., Gao, N., Deng, R., Sun, Q., Xu, Q.H., and Liu, X. (2013). Mechanistic investigation of photon upconversion in Nd^{3+}-sensitized core-shell nanoparticles. J. Am. Chem. Soc. *135*, 12608–12611.
43. Wang, F., Chen, X., Liu, D., Yang, B., and Dai, Y. (2012). Experimental and theoretical study of

pure and doped crystals: Gd_2O_2S, $Gd_2O_2S:Eu^{3+}$ and $Gd_2O_2S:Tb^{3+}$. J. Mol. Struct. *1020*, 153–159.

44. Hernandez-Adame, L., Palestino, G., Meza, O., Hernandez-Adame, P.L., Vega-Carrillo, H.R., and Sarhid, I. (2018). Effect of Tb^{3+} concentration in the visible emission of terbium-doped gadolinium oxysulfide microspheres. Solid State Sci. *84*, 8–14.

45. Liu, L., Wang, S., Zhao, B., Pei, P., Fan, Y., Li, X., and Zhang, F. (2018). Er^{3+} Sensitized 1530 nm to 1180 nm Second Near-Infrared Window Upconversion Nanocrystals for In Vivo Biosensing. Angew. Chem. Int. Ed. *57*, 7518–7522.

46. Chen, Q., Xie, X., Huang, B., Liang, L., Han, S., Yi, Z., Wang, Y., Li, Y., Fan, D., Huang, L., and Liu, X. (2017). Confining Excitation Energy in Er^{3+} -Sensitized Upconversion Nanocrystals through Tm^{3+} -Mediated Transient Energy Trapping. Angew. Chem. Int. Ed. *56*, 7605–7609.

47. Dorenbos, P. (2005). Mechanism of persistent luminescence in Eu^{2+} and Dy^{3+} codoped aluminate and silicate compounds. J. Electrochem. Soc. *152*, H107.